3D Microstructural Effects in Biphasic Steel Cutting

MARCO PICCININI and LAURENT HUMBERT
Laboratory for Computer-Aided Design and Production
Swiss Federal Institute of Technology Lausanne
CH-1015 Lausanne
SWITZERLAND

PAUL XIROUCHAKIS
Department of Design Manufacture and Engineering Management
University of Strathclyde
75 Montrose Street, Glasgow, G1 1XJ
UNITED KINGDOM

Paul.Xirouchakis@Strath.ac.uk https://www.strath.ac.uk/staff/xirouchakispaulprofessor/

Abstract: A three dimensional (3D) fully coupled thermal-mechanical analysis is presented in order to evaluate the influence of certain cutting parameters as well as dual phase microstructure on the orthogonal micro cutting process of steels (in particular, AISI 1045 steel), for which the size of heterogeneities is of the order of magnitude of the uncut chip thickness and tool edge radius. The simulated microstructure is composed of successive hexagonal close-packed layers with grain size control allowing to reproduce the desired fraction volume of the two considered constituents. Based on Johnson-Cook failure criteria inside the constitutive phases and a cohesive zone model along their interfaces, the numerical model is able to take into account both intra and inter granular damage initiation and evolution. Through an analysis of variance (ANOVA) method, a systematic study of the 3D microstructural effects and the relative effect of the pearlite-ferrite phases with respect to cutting settings (cutting speed, tool rake angle and tool radius) is carried out.

Key-Words: Micro-cutting, FEA, Inter/intra granular damage, 3D microstructure modeling

1 Introduction

While a plethora of analytical/numerical macro-scale models exist for predicting the material behavior during the cutting process (see for example the recent overview of Markopoulos [1]), there are considerably less studies, such as the precursory (two dimensional) analyses of Chuzhoy et al. [2][3][4], that simulate machined material by directly incorporating the workpiece microstructural composition, grain size, distribution and orientation. Thereafter, Simoneau et al. [5][6][7] focused on dimple and chip formation in AISI 1045 steel workpiece in plane strain conditions, stating that micro-scale cutting conditions may be achieved when the uncut chip thickness is less than the averaged size of the smallest grain type.

As reported by Dornfeld et al. [8], both surface finish and chip formation process can be affected by the crystallographic orientation of the grains at the micro-scale level, where the interaction with the tool edges may completely occur within a grain. Variations in the shear angle and cutting force have then been observed when cutting single crystals of beta brass for certain cutting directions with respect to the crystal orientation. Based on crystal plasticity theory, a microstructure –level cutting model recently proposed by Zhang et al. [9], was also able to capture the influence of the material microstructure on chip formation and surface finish.

In the present work, we aim at developing a three dimensional (3D) fully coupled thermal- stress model for two phase metals cutting (in particular, ferrite-pearlite steels) that explicitly integrates the material microstructure (as hexagonal close-packed structure) with both trans-granular and inter-granular damage evolution. Beside the use of Johnson-Cook (JC) shear failure model for critical plastic strain accumulation in individual grains, a cohesive zone model is activated to capture potential damage at grain interfaces. A factorial study and ANOVA are performed to rank the influence of the two-phase material with respect to

the following cutting parameters: cutting speed, tool rake angle and tool edge radius.

2 Numerical Model

2.1 Microstructural aspects and geometrical considerations

Modelling micro-cutting of heterogeneous materials, when cutting depths are in the order of the average grain size of the smallest grain type, requires a precise mapping of the constitutive phases that represents the actual microstructure. The cutting process is expected to be affected by the microstructure morphology, as measured by changes in the cutting and feed forces when the tool reaches and/or crosses the interfaces of the constitutive phases under certain conditions (Vogler et al. [10]).

In this work, ferritic-pearlitic hypo-eutectoid steels (with carbon content less than 0.77%) are chosen as representatives of two-phase ductile materials. They are composed of ferrite and pearlite, two distinct metallurgical constituents whose relative volume fractions depend on the carbon content. As discussed in Abouridouane et al. [11], pearlite, an alternating layer structure of ferrite and cementite, is the dominant phase in steels with higher carbon contents as C75 steels (with a carbon content of 0.75 wt.%). On the contrary for C05 steels, the ferrite phase appears quite exclusively with only a sparse apparition of pearlite at the grain corners. For carbon contents between 0.05% and 0.75%, the stronger pearlite grains are randomly distributed, surrounded by the relatively soft ferrite phase.

Following Abouridouane et al. [11], the synthetic workpiece microstructure considered here is characterized only by the volume fraction of the two constituents as well as a "reference" grain size, neglecting further microstructural features such as grain orientation, dislocation slip system within each randomly oriented grain, micro-defects and phase transformations. The heterogeneous microstructure is presented in Fig. 1 and is constituted of *N=3* layers of the same thickness having a hexagonal cell structure. This pattern is based on a regular hexagon with a circumcircle of radius r_h (i.e. the reference grain size) that is repeated (and cut if necessary) along the horizontal and vertical directions to map the entire rectangular workpiece domain. In the subsequent, the layer thickness t is taken as r_h (typically 40 μm). The geometric pattern is performed through in-house Python scripts that are executed within the (extended) scripting interface of the FE code ABAQUS (see ABAQUS [12]). Moreover, either ferrite or pearlite material definitions are assigned to each hexagonal cell through an efficient algorithm that ascertains the desired volume fraction of the ferrite phase. As shown in Fig. 1, all the cells of the same material are then agglomerated together to form the pearlite and ferrite phases distributed inside the rectangular workpiece domain of volume $l \times h \times Nt$ (fraction volume of 50 % for each constituent).

Tool and workpiece geometries as well as their relative (initial) position in the global working frame *(O, X, Y, Z)* are defined in Fig. 2. The tool profile is extruded along the *Z*-direction with the workpiece thickness Nt. As shown in the insert of Fig. 2, the edge radius r_e of the tool is defined through an internal (sketch) circle of the same radius, centred at *C*, that intersects perpendicularly the cutting and rake faces at points *B* and *D*, respectively. Line *O'C* represents the bisector of angle *O'DB*, where *O'* is the origin of the local frame (*x, y*). Local *x-y* and global *X-Y* planes are coincident and the initial coordinates of *O'* are set to $(l + r_e/2,\ h - h_0, 0)$ in the global frame (Fig. 2). The tool domain is bounded by an angular sector whose endpoints *A* and *E* belong to a limiting circle of radius r_t (tool size parameter in table 1), centred at point *O'*. In the local frame, the coordinates of *A* and *E* are given by

$$\begin{aligned} x_A &= r_t \cdot \cos\gamma', \quad y_A = r_t \cdot \sin\gamma' \qquad \gamma' = \pi/2 - \gamma \\ x_E &= r_t \cdot \cos\alpha, \quad y_E = r_t \cdot \sin\alpha \end{aligned} \tag{1}$$

where the positive angle γ' gives the orientation of the cutting face (AB) with respect to the horizontal *x*-axis. In the figure, the classical rake angle $\gamma = \pi/2 - \gamma'$ is depicted with a negative value. The clearance angle α orientates the clearance face (DE) with respect to *x*-axis $(\alpha < \gamma')$.

Introducing the angles $\alpha_1 = (\gamma' - \alpha)/2$ and $\alpha_2 = (\gamma' + \alpha)/2$ depicted in the insert of Fig. 2, the cutting depth is given by $h_c = h_0 - h_1$ where the height h_1 can be expressed as

$$h_1 = r_e \left(\frac{\sin\alpha_2}{\sin\alpha_1} - 1 \right) \tag{2}$$

indicating the local position of the horizontal tangent to the tool lower part at point C'.

Finally, the global coordinates of the reference point RP that serves to impose the tool velocity later are given by

$$\begin{aligned} X_{RP} &= l + r_e/2 + \left(x_A + x_E\right)/2 \\ Y_{RP} &= h - h_0 \quad + \left(y_A + y_E\right)/2 \\ Z_{RP} &= Nt/2 \end{aligned} \tag{3}$$

Note that in Fig. 2 it is rather the projection of RP that is depicted, located at the mid-length of the segment AE. The values of the previous parameters considered here are given in Table 1.

2.2 Material properties of the constitutive phases

General material parameters, including in particular thermal and elastic properties for an AISI 1045 workpiece and Tungsten carbide tool are shown in Table 2. These data are used for each of ferrite and pearlite phase, without distinction between the phases. The cutting process is generally extremely rapid and an uncoupled adiabatic analysis would be possible. However, a fully coupled thermal-stress analysis allows to simulate the evolution of the thermal field in the cutting tool. A compromise is to follow the approach of Mabrouki and Ridal [13] by setting the thermal conductivity λ of the machined materials to zero in order to stop dissipation.

The visco-plastic behaviour of each constitutive phase is modeled using the Johnson-Cook (JC) hardening law for which the yield equivalent (flow) stress $\bar{\sigma}$ depends multiplicatively on the equivalent plastic strain $\bar{\varepsilon}^p$, plastic strain rate $\dot{\bar{\varepsilon}}^p$, and temperature T as follows

$$\bar{\sigma} = \left(A + B\left(\bar{\varepsilon}^p\right)^n\right) \cdot \left(1 - \left(\frac{T - T_{trans}}{T_{melt} - T_{trans}}\right)^m\right) \cdot \left(1 + C \ln \frac{\dot{\bar{\varepsilon}}^p}{\dot{\varepsilon}_0}\right) \tag{4}$$

where $\dot{\varepsilon}_0$ is the reference strain rate, T_{melt} the melting temperature, T_{trans} the transition temperature (taken as room temperature here). In equation (4), the rheological parameters A, B, C, n and m stand for the initial yield stress, the hardening coefficient, the strain rate dependency, the work-hardening exponent and the thermal softening sensitivity, respectively. Below the transition (room) temperature, no temperature dependence on the yield stress is assumed. Phase-dependent material parameters used in the simulation for both materials are given in Table 3.

In addition, a bulk (isotropic) damage model should be considered to assess intragranular material separation. In this work, the Johnson-Cook (JC) damage initiation criterion, available in Abaqus/Explicit, is chosen. Fracture typically occurs when the equivalent plastic strain reaches a critical value expressed as

$$\bar{\varepsilon}_f^p = \left(d_1 + d_2 \exp\left(d_3 \frac{\sigma_m}{\sigma_{eq}}\right)\right)\left(1 + d_4 \ln \frac{\dot{\bar{\varepsilon}}^p}{\dot{\varepsilon}_0}\right)\left(1 + d_5\left(\frac{T - T_{trans}}{T_{melt} - T_{trans}}\right)\right) \tag{5}$$

where the same failure parameters d_1, d_2, d_3, d_4, d_5 are used for the two workpiece materials and summarized in Table 4. In Eq. (5), the equivalent (plastic) strain at failure $\bar{\varepsilon}_f^p$ depends on the ratio of the hydrostatic stress to equivalent Von Mises stress σ_m/σ_{eq}, the ratio $\dot{\bar{\varepsilon}}^p/\dot{\varepsilon}_0$ and temperature. The model is based on the value of the equivalent plastic strain at element integration points and failure occurs when the damage parameter D reaches 1. The element is then removed from the mesh upon failure. In the range $0 < D < 1$, damage manifests by the degradation of the elasticity as well as the softening of the yield stress. Damage evolution is specified in terms of the fracture energy G_f (per unit area) that is set to zero for a rapid failure after damage onset (see Table 4).

2.3 Finite Element explicit model

In the FE explicit model, the workpiece is modelled as a two-phase damageable viscoplastic 3D block as discussed previously. For each phase of the workpiece, a free meshing technique is employed using 10-node modified thermally coupled second-order tetrahedrons (C3D10MT). The tool is modelled as an undamageable elastic body with a non-zero conductivity (while it is set to zero for the workpiece materials) and meshed using hourglass control and reduced integration 8-node hexahedric elements with trilinear displacement and temperature (C3D8RT) of constant size L_e. A mapped meshing is built using the media axis algorithm in Abaqus, with an element size varying from $L_e/2$ at the tool edge to L_e in the other exterior edges.

For the fully coupled thermal-stress analysis, thermal and mechanical solutions are obtained in Abaqus/Explicit using forward-difference and central-difference (Newmark) integration schemes

that are conditionally stable. The time increment size Δt is conditioned by the element size L_e as well as the thermal diffusivity of the constitutive materials $\alpha = \lambda/(\rho c_p)$, where the material parameters are defined in Table 2. The stability requirement is expressed as (ABAQUS [12])

$$\Delta t \leq \frac{L_e^2}{2\alpha} \quad (6)$$

Regarding to equation (6), the mesh size clearly affects both computational speed and solution convergence. Strictly speaking, it is the size of the smallest element in the mesh that is considered in equation 6, avoiding the use of focusing meshes that may lead to inappropriate very small elements. Dense meshes (i.e. small element size L_e) result in small time increments are computationally expensive and time consuming. Selecting a constant element size L_e of 8.5μm and a mass scaling technique, convergent solutions have been successfully obtained after approximately 8 hours of computing time when cutting the three-layer workpiece in Fig. 1 (and Fig. 4a) over a length of $750\,\mu m$ (two-third of the workpiece length). Smallest time increments of about $5 \cdot 10^{-10} s$ are typically recorded during the simulation.

2.3.1 Boundary conditions

The nodes of the end-left surface of the workpiece are constrained in *X* direction while all active degrees of freedom are constrained for the bottom nodes of the workpiece. Symmetry conditions about the *Z*- axis are also imposed at the front and rear faces of the workpiece. The tool motion is modelled as follows: all the nodes of the upper surface (line AE in Fig. 2) are linked rigidly to the reference point/node (RP) that is defined through equation (3). Tool displacement is enforced in the cutting direction *X* by constraining the rotation in the *X*-*Y* plane as well as displacement along the *Y* direction at the reference node. A constant cutting speed V_c is also applied at RP (see Table 1) in the cutting direction. Initial thermal conditions are imposed by applying a room temperature inside the workpiece and tool domains.

2.3.2 Mechanical/thermal interactions

Two kinds of interactions are specified through the general contact algorithm available in Abaqus/Explicit. Firstly, the tool-workpiece interaction is prescribed. Because of the high tool velocity and the small time period for the cutting process, only thermal conduction is considered at the tool-workpiece surface, neglecting the other modes of heat mode transfer (radiation and convection). An inelastic heat fraction coefficient of 0.9 is adopted, as reported in the literature. At the tool-workpiece interface, all the dissipated energy is assumed to be converted into heat and a thermal contact conductance of $10^4\ W \cdot m^{-2} \cdot C^{-1}$ ($W.m^{-2}C^{-1}$) as well as a heat partition coefficient of 0.75 are selected (see Table 5).

Pearlite-ferrite interfacial properties are modelled using a cohesive zone model for which material separation and fracture are governed by a cohesive law that specifies the traction-separation constitutive behaviour (Jadhav and Maiti [14]; Mohammed et al. [15]). Damage initiation criteria is defined in terms of the three peak traction components $t_n^0, t_t^0 \left(n = I,\ t = I, III\right)$ with the respective separation components at damage onset δ_n^0, δ_t^0. As illustrated in Fig. 3, cohesive contact is imposed at the external surfaces of the grains delimiting the constitutive phase domains. After damage onset, the interface material begins losing its stifness and failure occurs at the separation at fracture δ_n^f, δ_t^f (see Fig. 3). In this model, a linear damage evolution is specified in terms of a common value $G_C = G_{IC} = G_{IIC} = G_{IIIC}$ of the fracture energy for the three damage modes. This critical energy is dissipated during the damage process (i.e. the area under the traction-separation curves). Data for both the peak tractions and fracture energy are extracted from Jadhav and Maiti [14] and reported in Table 5.

The tangential behavior at both tool-workpiece and constitutive materials interface is driven by a Coulombic friction behavior with a (common) value for the coefficient friction given in Table 5. Hard contact is considered in the normal direction.

3 Parametric Study

The simulations were performed on the Bellatrix cluster at EPFL, that is composed by 424 compute nodes, each with: 2 Sandy Bridge processors running at 2.2 GHz, with 8 cores each (i.e. 16 cores per compute node), 24 GB of RAM and Infiniband QDR 2:1 connectivity.

3.1 Effect of microstructure on the cutting and feed forces

Fig. 4a shows a 0.75 mm cutting length of a part of

heterogeneous composition with the size $l \times h \times 3t = 1020 \times 242 \times 120\,\mu m^3$ (volume fraction of 50% for the constituents) with the cutting parameters given in Table 1. This corresponds to a total machining time of 0.375 millisecond. Also indicated is the equivalent plastic strain (PEEK).

Fig. 4b gives a comparison of the cutting and feed forces obtained for three microstructural pearlitic-ferritic (P-R) realizations, individual pearlite (P) and ferrite (F) phases as well as homogenenous AISI 1045 material. Steady–state cutting conditions are readily obtained after 0.2 mm of cutting length.

3.2 ANOVA study

Subject: analysis of the influence of cutting parameters and multi-phase material modelling, through a full factorial study and ANOVA.

Goal: to rank the influence of a multi-phase material with respect to cutting settings (cutting speed, tool rake angle and tool radius).

Method: A full factorial study is designed considering 4 factors and 2 levels each, as summarized in Table 6. The table of "experiments" includes 16 simulations (runs) with a complete combination of these factors (Table 7).

Basically, two FE models of orthogonal cutting were generated: a model characterized with homogenized material properties of steel AISI 1045 and a two-phase model characterized with pearlite and ferrite properties (Abouridouane [11]).

Workpiece domain of size $l \times h \times 3t = 2460 \times 242 \times 120\,\mu m^3$ (Table 1).

These models were used as reference and adapted by changing the remaining factors (tool speed, rake angle and tool radius) for all simulation. Thus, it is worth noticing that only one pattern of grain distribution was used, and no influence of different granular distribution was in this analysis.

Outputs: Different outputs were investigated. Both mean and standard deviations were extrapolated as representative of the average and fluctuation of the output, respectively.

Tool outputs:

1) **Cutting force**: that is the reaction force acting along the direction of cut. The mean and the standard deviation of this variable were estimated on the stable solution (i.e. ignoring the transitory initial phase).
2) **Feed force**: that is the reaction force acting perpendicularly to the machined surface. The mean and the standard deviation of this variable were estimated on the stable solution (i.e. ignoring the transitory initial phase).
3) **Temperature**: that is the temperature reached in the tool due the contact with the workpiece. Mean and standard deviation were computed on the tool frontal surface (i.e. the surface along the direction of cut, including the tool radius, see Fig. 5a). The values adopted for the analysis were the ones reached at the end of the cutting path.

Workpiece outputs:

4) **PEEQ**: that is the plastic equivalent strain. Average and standard deviation were estimated in a region of interest immediately in front of the tool (Fig. 5a).
5) **TEMP**: that is the temperature reached in the workpiece due to plastic deformation. Average and standard deviation were estimated in a region of interest immediately in front of the tool (Fig. 5a).

Analysis of variance

Analyses of variance (ANOVA) were performed on all outputs to highlight the influence of each main factor (material, rake angle, cutting speed and tool radius) and their first order interactions. Two type of output are analysed (Fig. 5b):

- The variable mean μ: i.e. mean value at which the output stabilizes (reaches a plateau).
- The variable standard deviation σ: that is representative of the variable fluctuation along the stabilized path.

The effects are estimated as percentage of the average value of the whole set of simulation. Their absolute value is ranked to establish which factor or interaction is more relevant.

4 Results and Discussion

Two type of graphic representation are shown:

- Trends of output with respect to tool displacement. All 16 simulations are with a legend that identifies each configuration.
- Histograms showing percent variations of μ and σ due to factors and interaction. Absolute variations are rank in decreasing order. Since the main interest concerns the influence of the material characterization, the material factor is highlighted in black and its first order interaction in grey.

4.1 Cutting force

Fig. 6 shows the trend of the cutting force with

respect to the tool displacement, computed for all 16 simulations. Observations:

- The force is stabilized after 0.3 mm in a range between 18-25 N.
- All results are grouped; none of the factor has a clear influence.
- The reaction force estimated in run 8 (Homogeneous AISI 1045, rake angle = 7 deg, cutting speed = 2000m/s, tool radius = 0.05mm) did not reach a plateau (Fig. 7).

Fig. 8 shows the variations of the cutting force mean (top) and standard deviation (bottom) generated by main factors and first order interactions.

Observations concerning the mean:

- Absolute variations do not overcome 5%, which highlights that the average cutting force is scarcely affected by the selected factors and levels.
- Machining parameters (rake angle, cutting speed and tool radius) influence the cutting force more than the material and its interactions.
- It seems that modelling steel AISI 1045 with homogenized or multi-phase materials does not significantly affect the predicted cutting force mean.

Observations concerning the standard deviation:

- Absolute variations reach ±30%, which highlights that the cutting force fluctuation is largely affected by the selected factors.
- An increase of cutting speed provokes an increase of the force fluctuation. It can be explained by a faster plasticisation/deletion of finite elements that induces more vibrations.
- An increase of tool radius provokes an increase of the force fluctuation. The higher is the tool radius, the less sharper is the tool and the most unstable is the cutting process.
- Adopting a multi-phase material involves a reduction of the fluctuation.

4.2 Feed force

Fig. 9 shows the trend of the feed force with respect to the tool displacement, computed for all 16 simulations. Observations:

- Force trends are stabilized after 0.2 mm and they cover a wide range (5-16 N), which means that this output is highly influenced by the selected set of parameters.
- All trends are stable, even Run 8 which provided an unstable cutting force.

Fig. 10 shows the variations of the feed force mean (top) and standard deviation (bottom) generated by main factors and first order interactions.

Observations concerning the mean:

- Two factors have the higher influence (±20%): rake angle and tool radius.
- Adopting a positive rake angle provokes a 19% decrease of the feed force. Indeed, positive rake angles involve a sharper tool and a consequently easier cut.
- Increasing the tool radius induces a 18% increase of the feed force. Indeed, a tool with a bigger radius is less sharp and leads to higher reaction forces.
- Adopting a multi-phase material causes a negligible effect with respect to machining parameters (rake angle, cutting speed and tool radius).

Observations concerning the standard deviation:

- Absolute variations reach ±20%, which highlights that the feed force fluctuation is largely affected by the selected factors.
- Increases of cutting speed and tool radius induce more fluctuations.
- First order interactions involving the multi-phase material provoke a reduction of the force fluctuation. This result is consistent with the corresponding cutting force results.

4.3 Tool temperature

Fig. 11 shows the trend of the tool temperature with respect to the tool displacement, computed for all 16 simulations. Observations:

- Similarly to the cutting force, all trends are grouped. None of the factor has a predominant influence.
- At the end of the simulations the mean temperature reached 70-120° and is still increasing. A longer cutting path and tool heat dissipation should be accounted to predict a converged solution.
- Standard deviations are really large. Indeed, only a small part of the tool frontal surface (Fig. 5a) is actually in contact with the tool. The rest experienced no temperature variations.

Fig. 12 shows the variations of the tool temperature mean (top) and standard deviation (bottom) at the end of the simulations.

Observations concerning the mean:

- Absolute variations do not overcome 7%, which highlights that the tool temperature is

scarcely affected by the selected factors and levels.
- Adopting a multi-phase material induces a small reduction of the mean temperature, as well as increasing the tool radius.
- Increasing cutting speed or rake angle provokes a small increase of the mean temperature.

Observations concerning the standard deviation:
- Similarly to the mean temperature, cutting speed, rake angle and material are the factors that mostly influence the temperature fluctuation: the first two increases it, while a multi-layer material decreases the tool temperature spread.

4.4 Workpiece temperature

Fig. 13 shows the trend of the workpiece temperature with respect to the tool displacement, computed for all 16 simulations in the region of interest shown in Fig. 5a. Observations:
- The average temperature is stabilized after 0.4 mm in between 300-400 °C, thus not reaching phase-transition temperatures - steel (730 °C).
- All results are grouped, no clear influence is visible except wider standard deviations due to multi-phase material (blue) with respect to the homogenized one (red).

Fig. 14 shows the variations of the workpiece temperature mean (top) and standard deviation (bottom).

Observations concerning the mean:
- Absolute variations do not overcome 7%, which highlights that the workpiece temperature is scarcely affected by the selected factors and levels.
- The only relevant factor is the rake angle: if it is positive, lower temperatures are reached in the workpiece.

Observations concerning the standard deviation:
- The material has a strong effect on workpiece temperature fluctuations. In detail, adopting a multi-phase material increases the temperature fluctuation of about 20% with respect to homogenized models.
- That means that assuming a homogeneous material at this scale may involve inaccurate predictions of temperature-related phenomena (e.g. phase transitions).

4.5 Workpiece plastic equivalent strain

Fig. 15 shows the trend of the workpiece plastic equivalent strain with respect to the tool displacement, computed for all 16 simulations in the region of interest shown in Fig. 5a. Observations:
- The average plastic equivalent strain is stabilized after 0.6 mm in between 1-1.5.
- All results are grouped; no clear influence is visible except wider standard deviations due to multi-phase material (blue) with respect to the homogenized one (red).

Fig. 16 shows the variations of the plastic equivalent strain (top) and standard deviation (bottom).

Observations concerning the mean:
- Absolute variations do not overcome 7%, which highlights that the workpiece plastic strain is scarcely affected by the selected factors and levels.
- Similarly to the workpiece temperature, the only relevant factor is the rake angle: if it is positive, lower strains are reached in the workpiece.

Observations concerning the standard deviation:
- The material and the rake angle have a strong effect on fluctuations of the workpiece plastic strain.
- Adopting a multi-phase material increases the workpiece plastic strain fluctuation of about 15% with respect to the homogenized model. On the contrary, adopting a positive rake angle decreases the plastic strain.
- Interestingly, the interaction of these two factors (M-A) has scarce effect.

5 Conclusion

The main objective of this paper is to report the influence of cutting parameters (cutting speed, tool rake angle and tool radius) during the orthogonal micro-cutting process of a dual-phase (ferritic-pearlitic AISI 1045 steel) material finite element model taking into account of the three dimensional (3D) effects. A full factorial simulation study was undertaken together with a corresponding analysis of variance (ANOVA) on the output variables (cutting force, feed force, tool & workpiece temperature and workpiece plastic equivalent strain).

The main conclusions of this study are the following:
- Adopting a dual-phase material model does not significantly affect the prediction of the mean of all output variables;
- The most significant influence on the mean is a ±20% variation of the mean feed force due to the rake angle and tool radius variations;

all other mean output variations do not exceed 7% considering all factors and levels;

- Adopting a dual-phase material model results in a reduction of the standard deviation fluctuation regarding the cutting and feed forces as well as the tool temperature with respect to the homogenized models;
- Adopting a dual-phase material model results in an increase of the standard deviation fluctuation regarding the workpiece temperature and plastic equivalent strain of about 20% to 15% respectively with respect to the homogenized models.

Future work will focus in correlating the above observations with regard to the corresponding chip formation process. Furthermore, variations of the sizes of the grains and distributions will be studied regarding their effect on the outputs.

References:

[1] Markopoulos, A. P. (2013) Finite Element Method in Machining Processes. Springer, London, Heidelberg, New York, Dordrecht.

[2] Chuzhoy, L.; DeVor, R.E.; Kapoor, S.G.; Bamman, D.J. (2002) Microstructure-Level Modelling of Ductile Iron Machining. ASME Journal of Manufacturing Science and Engineering, 124: 162-169.

[3] Chuzhoy, L.; DeVor, R.E.; Kapoor, S.G.; Beaudoin, A. J.; Bamman D.J. (2003) Machining Simulation of Ductile Iron and Its Constituents, Part1: Estimation of Material Model Parameters and Their Validation. ASME Journal of Manufacturing Science and Engineering, 125: 181-191.

[4] Chuzhoy, L.; DeVor, R.E.; Kapoor, S.G. (2003) Machining Simulation of Ductile Iron and Its Constituents, Part2: Numerical Simulation and Experimental Validation of Machining. ASME Journal of Manufacturing Science and Engineering, 125: 192-201.

[5] Simoneau, A.; Ng, E.; Elbestawi, M.A. (2006) Surface defects during microcutting. International Journal of Machine Tools and Manufacture, 46: 1378-1387.

[6] Simoneau, A.; Ng, E.; Elbestawi, M.A. (2006) The effect of microstructure on chip formation and surface defects in microscale, mesoscale and macroscale cutting of steel. CIRP Annals – Manufacturing Technology, 55 (1): 97-102.

[7] Simoneau, A.; Ng, E.; Elbestawi, M.A. (2007) Grain size and orientation effects when microcutting AISI 1045 steel. CIRP Annals - Manufacturing Technology, 56 (1): 57-60.

[8] Dornfeld, D.A.; Oliveira, J.F.G.; Lee, D.; Valente, C.M.O. (2003) Analysis of Tool and Workpiece Interaction in Diamond Turning Using Graphical Analysis of Acoustic Emission. CIRP Annals – Manufacturing Technology, 52 (1): 479-482.

[9] Zhang, Y.; Mabrouki, T.; Nelias, D.; Courbon C.; Rech, J.; Gong , Y. (2012) Cutting simulation capabilities based on crystal plasticity theory and discrete cohesive elements. Journal of Materials Processing Technology, 212: 936-953.

[10] Vogler, M.P.; DeVor, R. E.; Kapoor, S.G. (2003) Microstructure-Level Force Prediction Model for Micro-milling of Multi-Phase Materials. ASME Journal of Manufacturing Science and Engineering, 125: 202-209.

[11] Abouridouane, M.; Klocke, F.; Lung, D.; Adams, O. (2012) A new 3D multiphase FE model for micro cutting ferritic- pearlitic carbon steels. CIRP Annals – Manufacturing Technology, 61: 71-71.

[12] ABAQUS (2014). Abaqus Scripting User's Guide Version 6.14. Dassault Systems.

[13] Mabrouki, T.; Rigal, J.F. (2006) A contribution to a qualitative understanding of thermo-mechanical effects during chip formation in hard turning. Journal of Materials Processing Technology, 176: 214-221.

[14] Jadhav, D.N.; Maiti S.K. (2010) Characterization of stable crack growth through AISI 4340 steel using cohesive zone modeling and CTOD/CTOA criterion, 240: 713-721.

[15] Mohammed, W.M.; Ng, E.; Elbestawi, M.A. (2012) Modeling the effect of compacted graphite iron microstructure on cutting forces and tool wear, 5:87-101.

[16] Courbon, C.; Mabrouki, T.; Rech, J.; Mazuyer, D.; D'Eramo, E. (2011) New thermal issues on the modelling of tool-workpiece interaction: application to dry cutting of AISI 1045 steel. Advanced Materials Research, 223: 286-295.

[17] Duan, C.Z.; Dou, T.; Cai, Y.J.; Li, Y.Y. (2011) Finite Element Simulation and Experiment of Chip Formation Process during High Speed Machining of AISI 1045 Hardened Steel. AMAE Production and Industrial Engineering, 02 (01): 28-32.

6 Figures

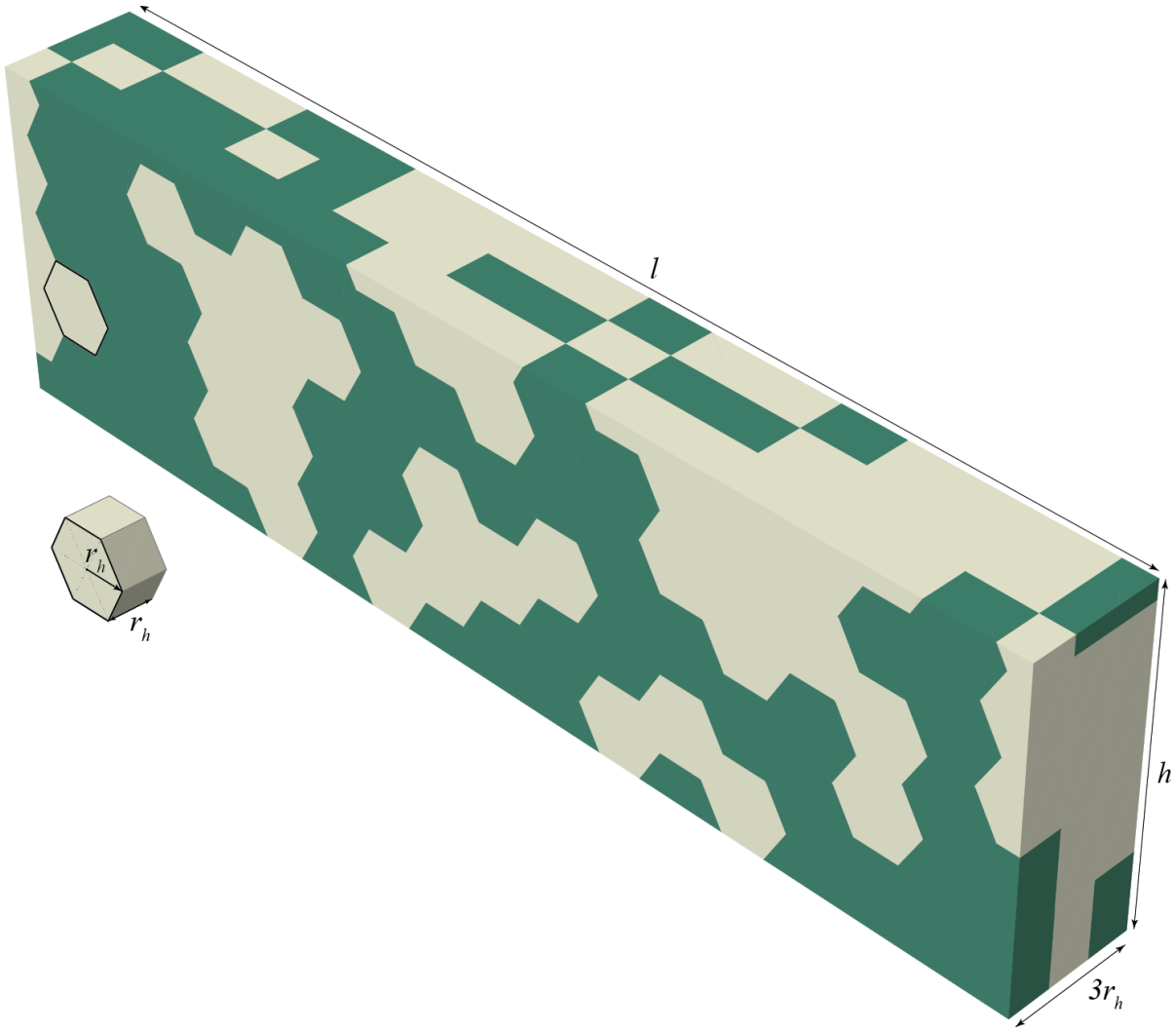

Fig. 1 Arrangement of three layers of hexagonal unit cells of size $t = r_h = 40\mu m$ forming the pearlitic (green) and ferritic (white) phases of the workpiece domain, with a volume fraction of 50% for each phase. Representative volume $l \times h \times 3t = 1020 \times 242 \times 120\,\mu m^3$ (see Table 1).

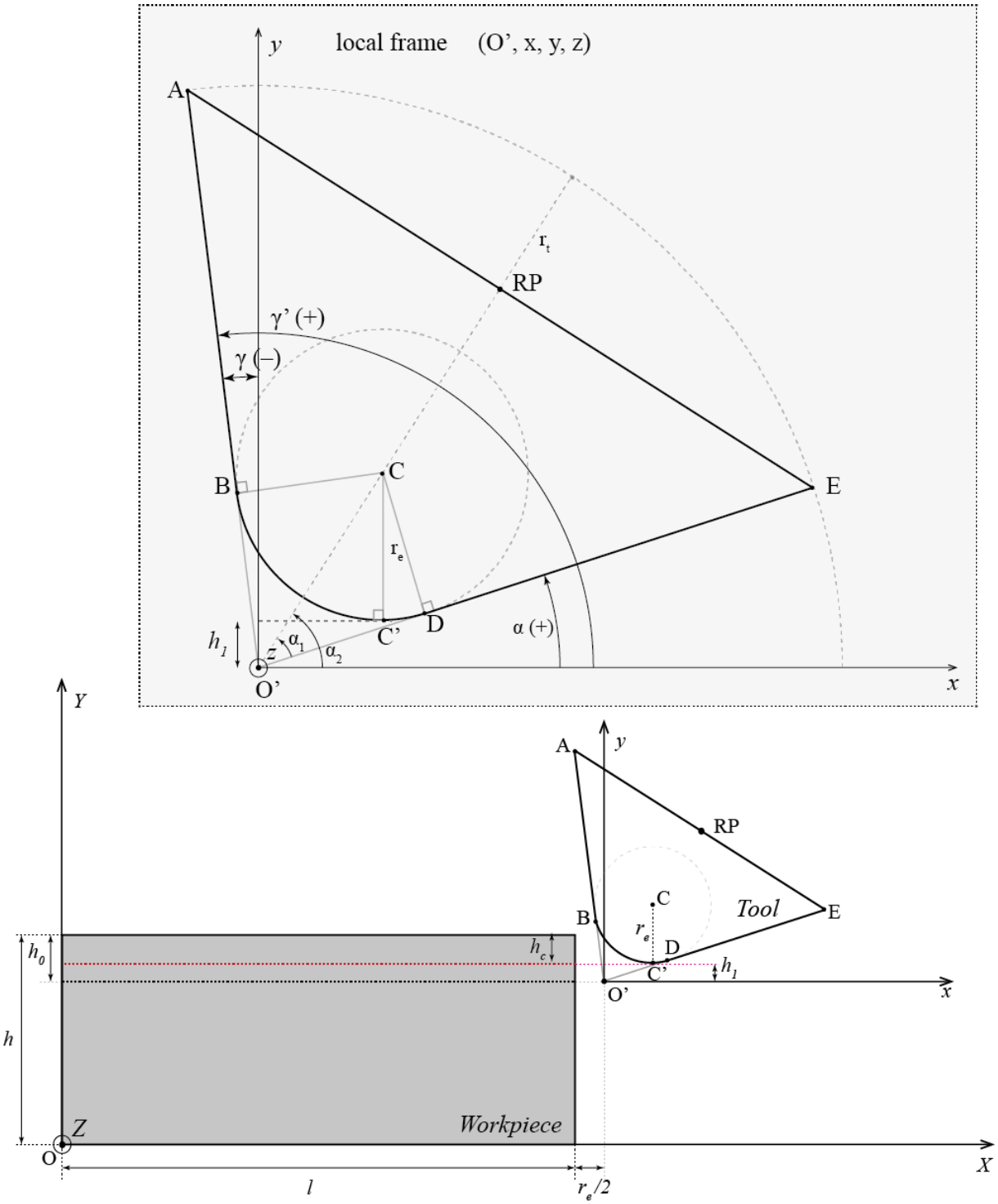

Fig 2 Initial position of the tool in the global frame and cutting depth h_c definition. In the insert, details of the tool geometry for a negative rake angle γ showing also the reference point (RP) location.

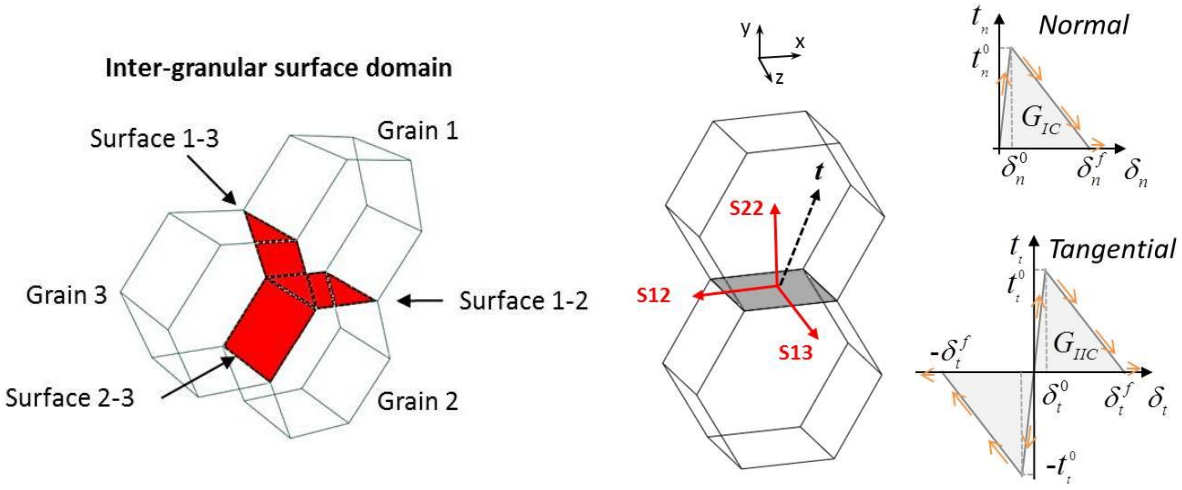

(a) (b)

Fig. 3 Inter-granular surface domain: (a) example of grains' boundaries and (b) Bilinear traction-separation laws in tension and shear

(a)

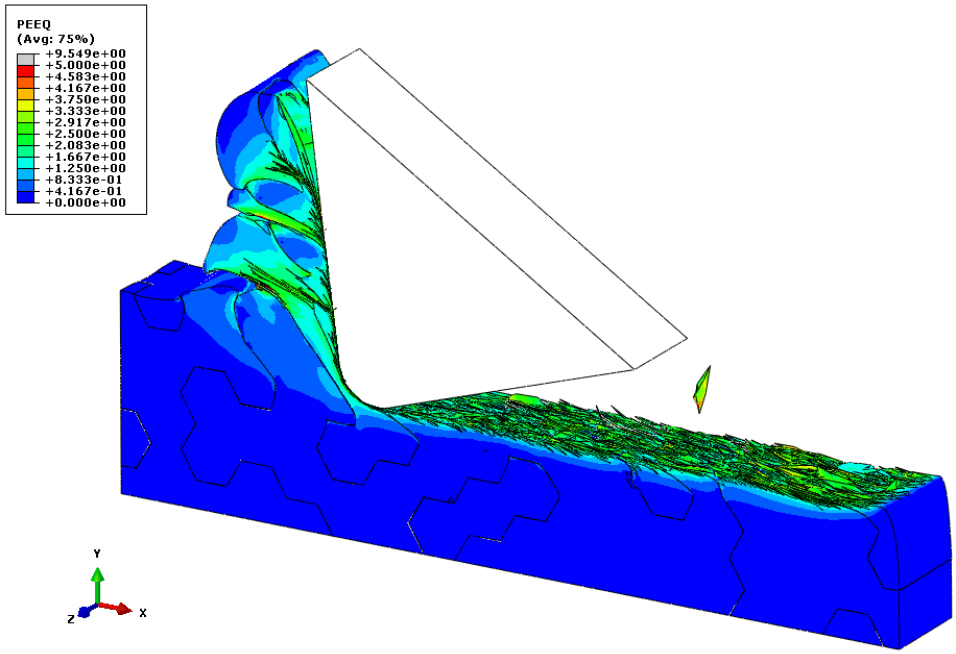

(b)

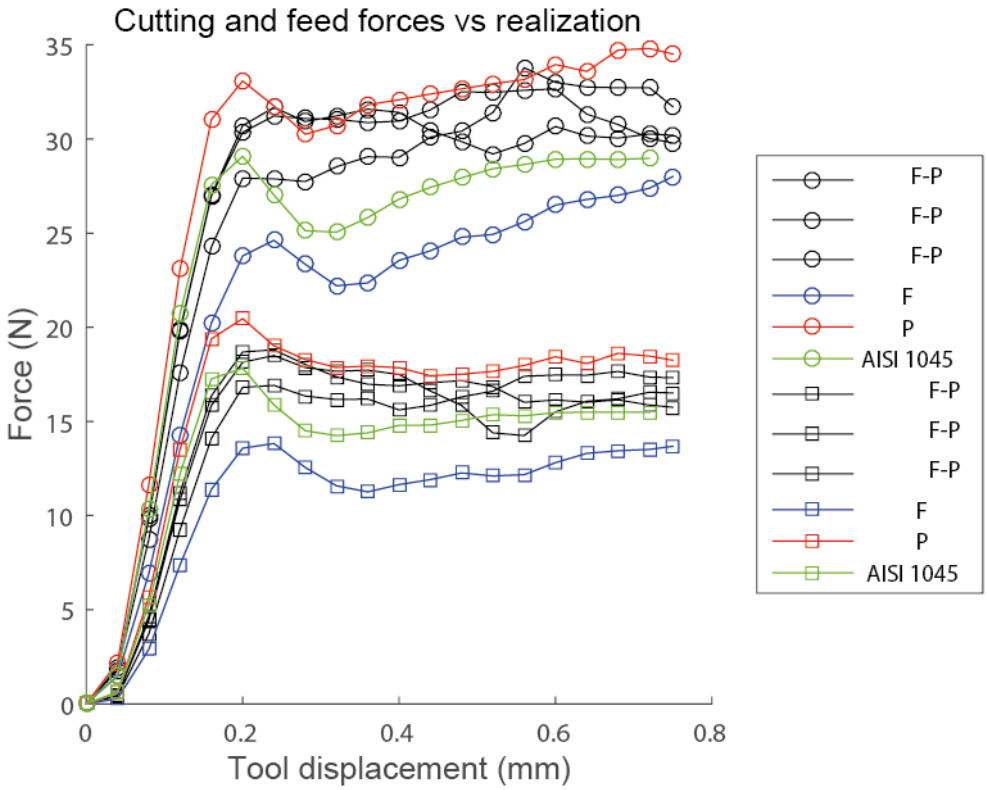

Fig. 4 (a) Cutting length of 750 μm of a heterogeneous ferrite-pearlite workpiece (volume fraction of 50%) with cutting parameters in Table 1 - Equivalent plastic strain (PEEK) (b) Comparison of cutting and feed forces for heterogeneous and homogeneous steel materials

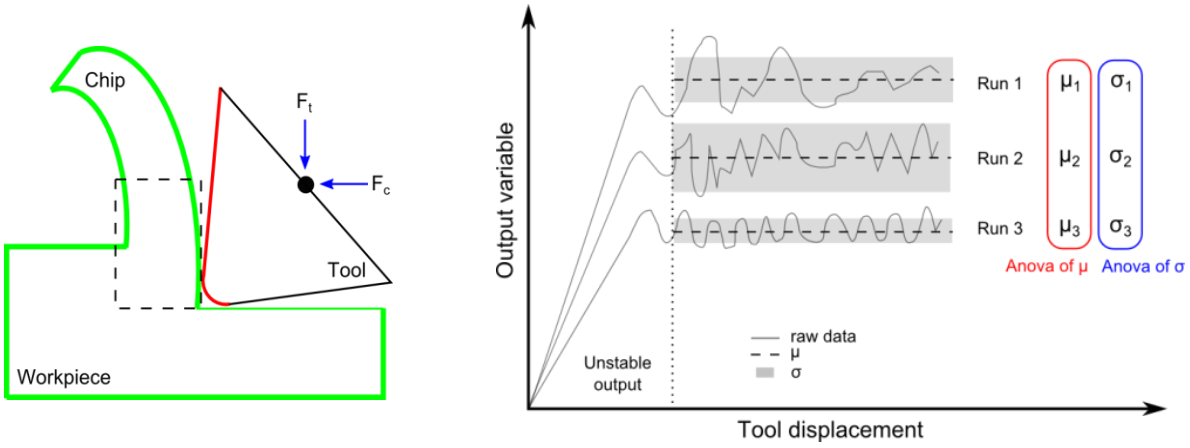

(a) (b)

Fig. 5 (a) 2D representation of the cutting FE model. The tool temperature is monitored on the frontal face of the tool (red). Workpiece outputs are averaged on the nodal values included in the hashed area. Feed and cutting forces (*Ft* and *Fc*) are monitored through a reference point. (b) Example of data collection: mean (μ) and standard deviation (σ) of the stable solution are computed for each simulation (run) and processed through ANOVA to highlight the factors influence on the stabilized output and its fluctuation, respectively.

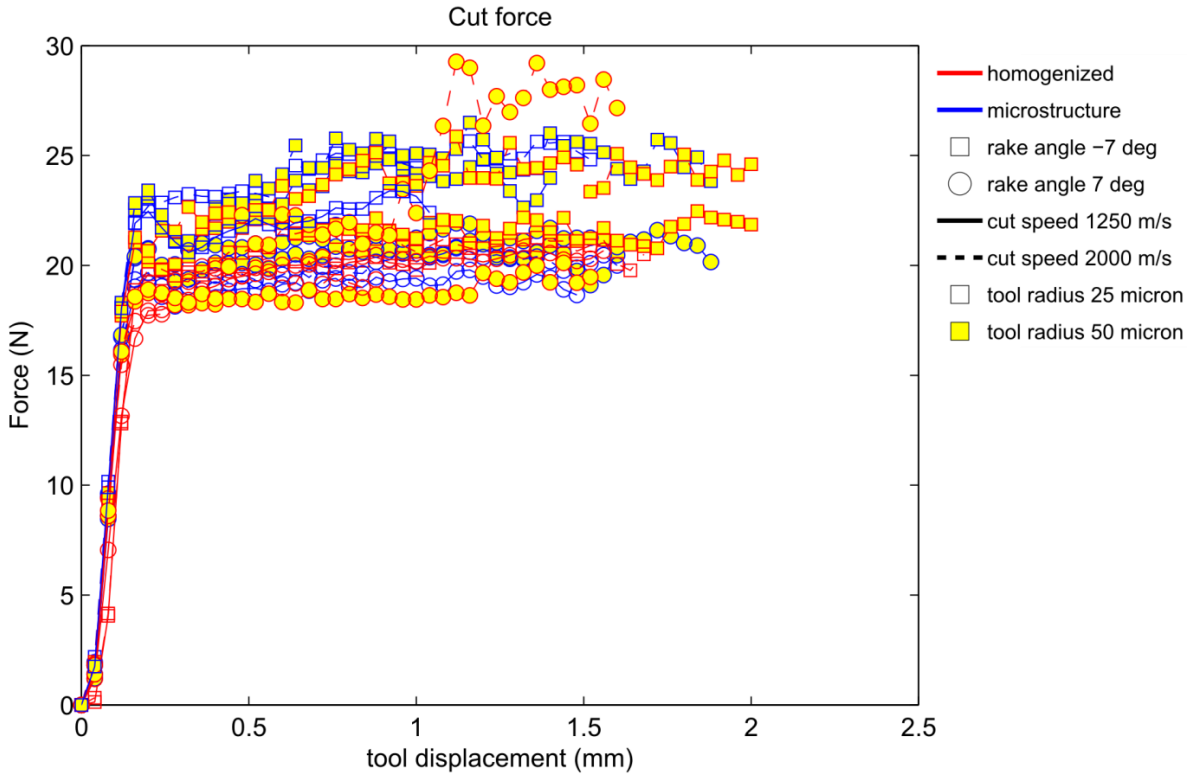

Fig. 6 Trend of the cutting force plotted versus the tool displacement.

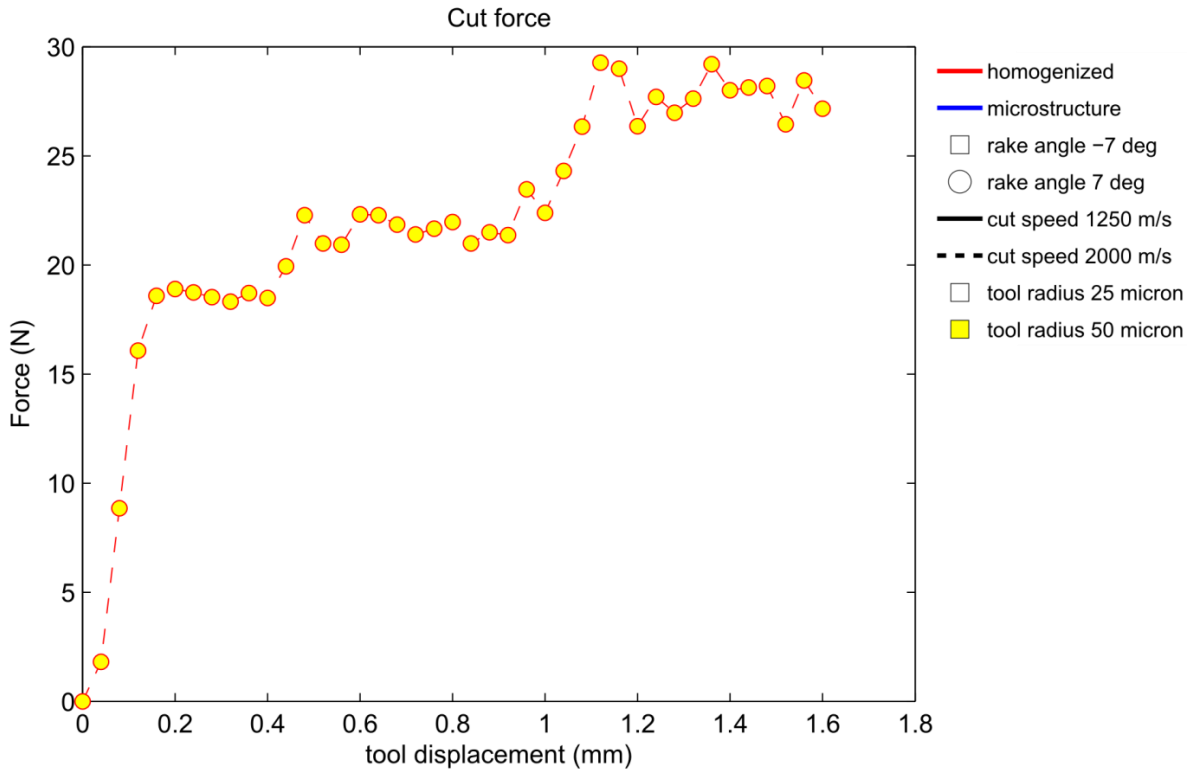

Fig. 7 Trend of the cutting force plotted versus the tool displacement for run 8 (Homogeneous AISI 1045, rake angle = 7 deg, cutting speed = 2000m/s, tool radius = 0.05mm).

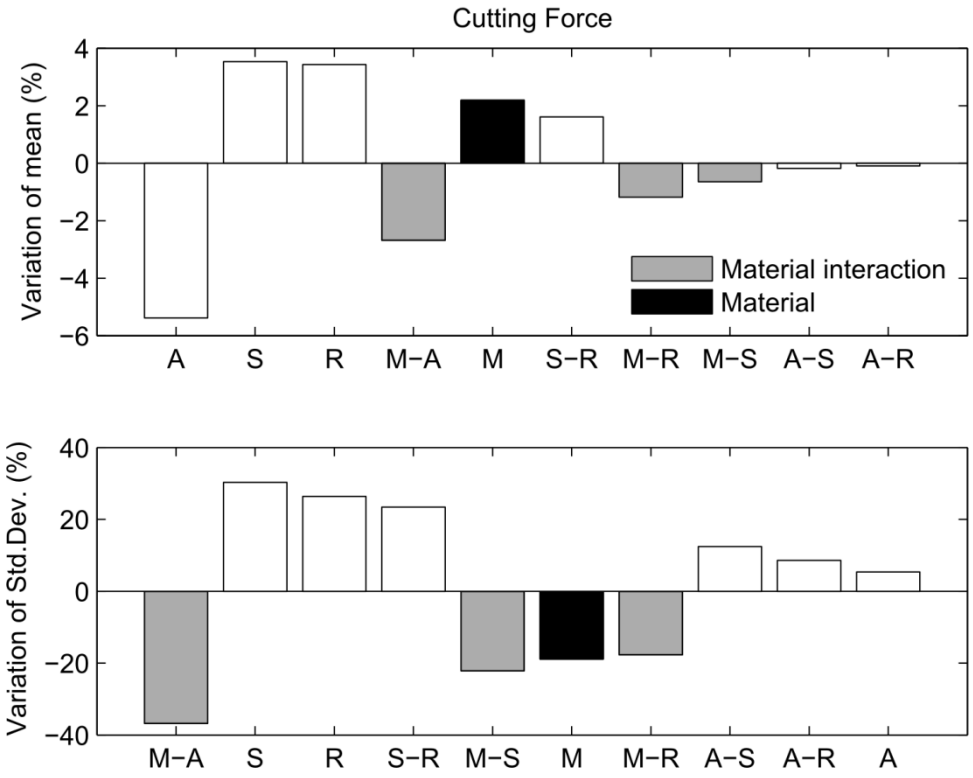

Fig. 8 Effects of main factors and their interactions on the cutting force mean (top) and standard deviation (bottom). Material = M, rake angle = A, cutting speed = S and tool radius = R. Absolute variations are rank in decreasing order from left to right.

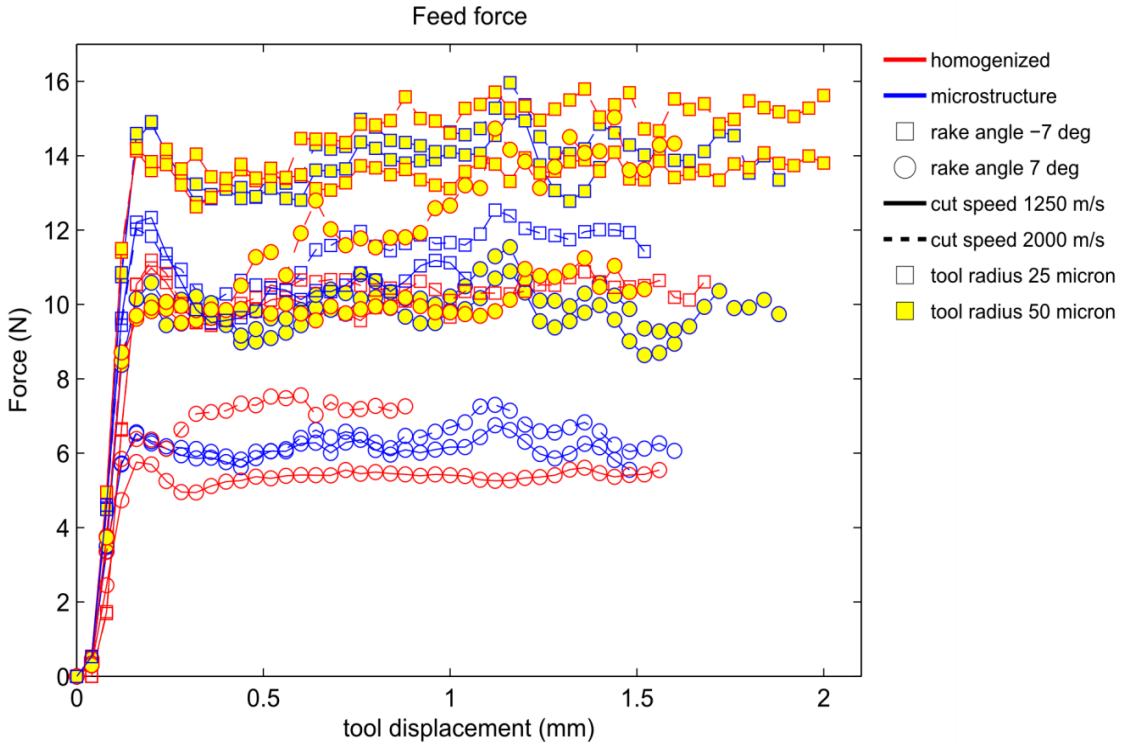

Fig. 9 Trend of the feed force plotted versus the tool displacement.

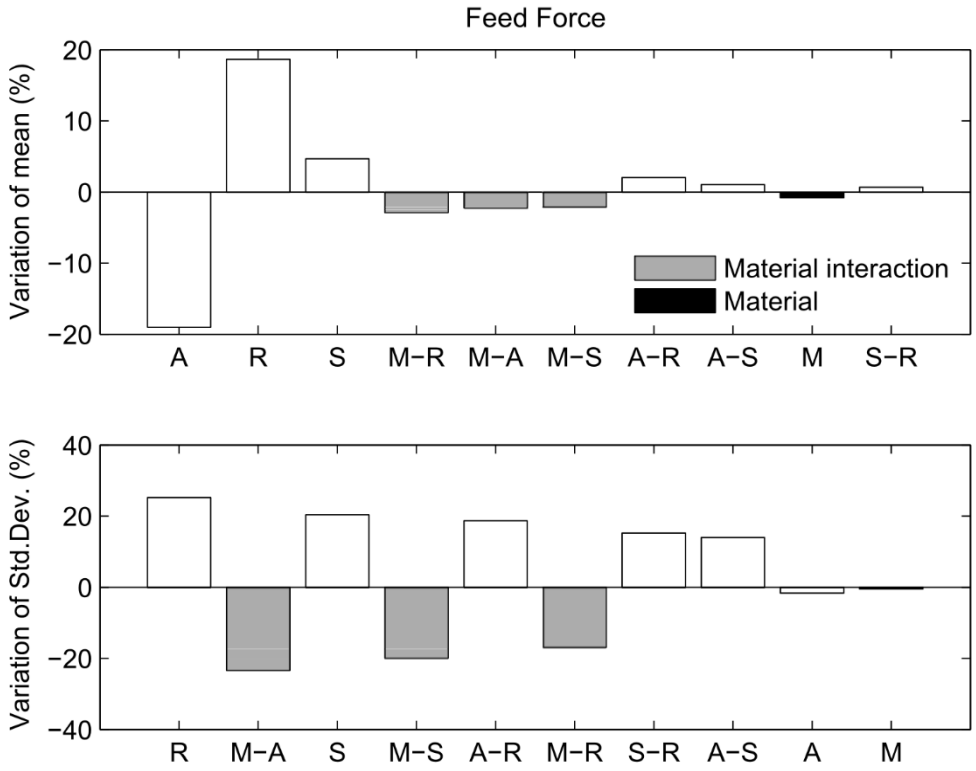

Fig. 10 Effects of main factors and their interactions on the feed force mean (top) and standard deviation (bottom). Material = M, rake angle = A, cutting speed = S and tool radius = R. Absolute variations are rank in decreasing order from left to right.

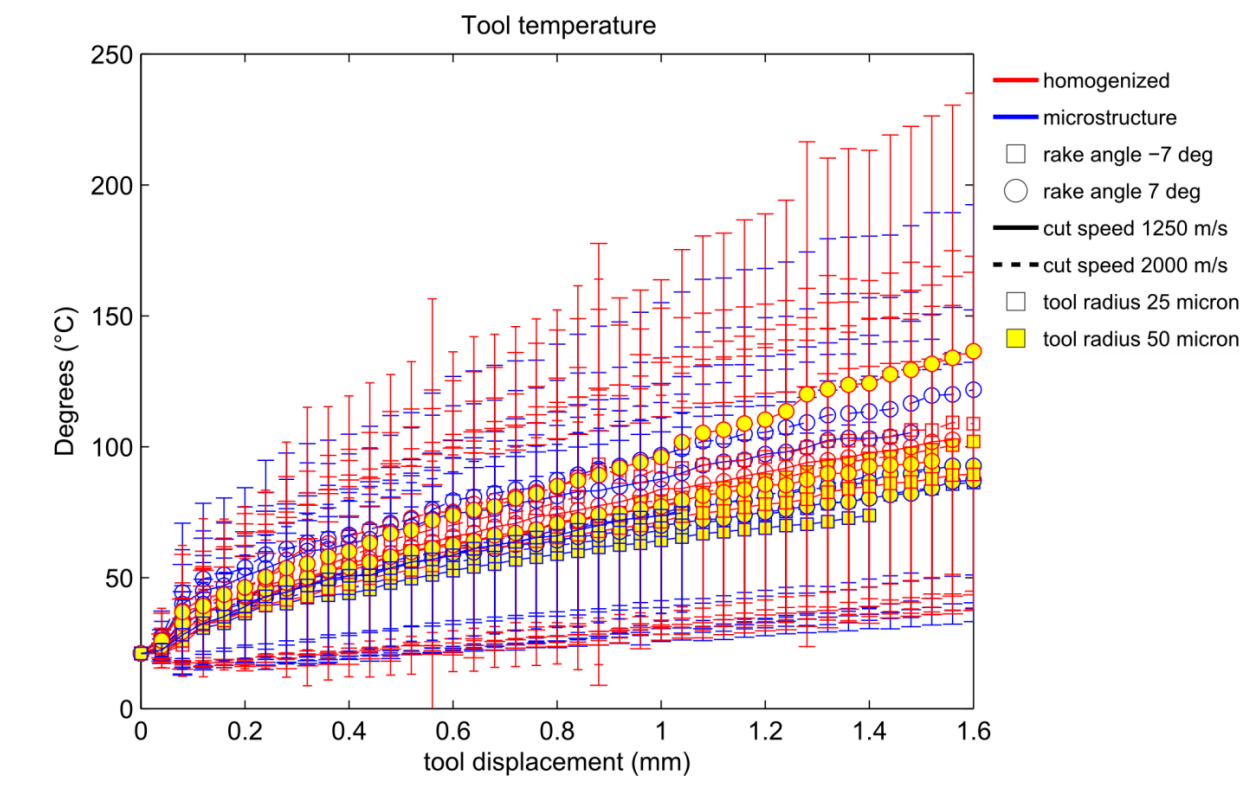

Fig. 11 Trend of the tool temperature plotted versus the tool displacement.

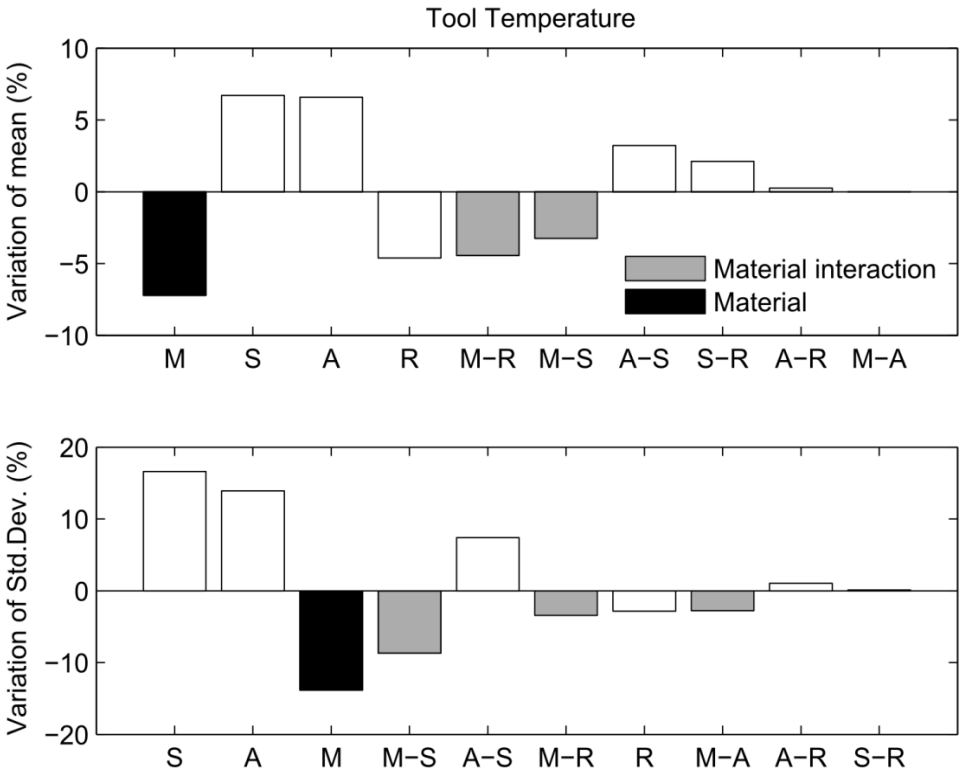

Fig. 12 Effects of main factors and their interactions on the mean tool temperature (top) and standard deviation (bottom). Material = M, rake angle = A, cutting speed = S and tool radius = R. Absolute variations are rank in decreasing order from left to right.

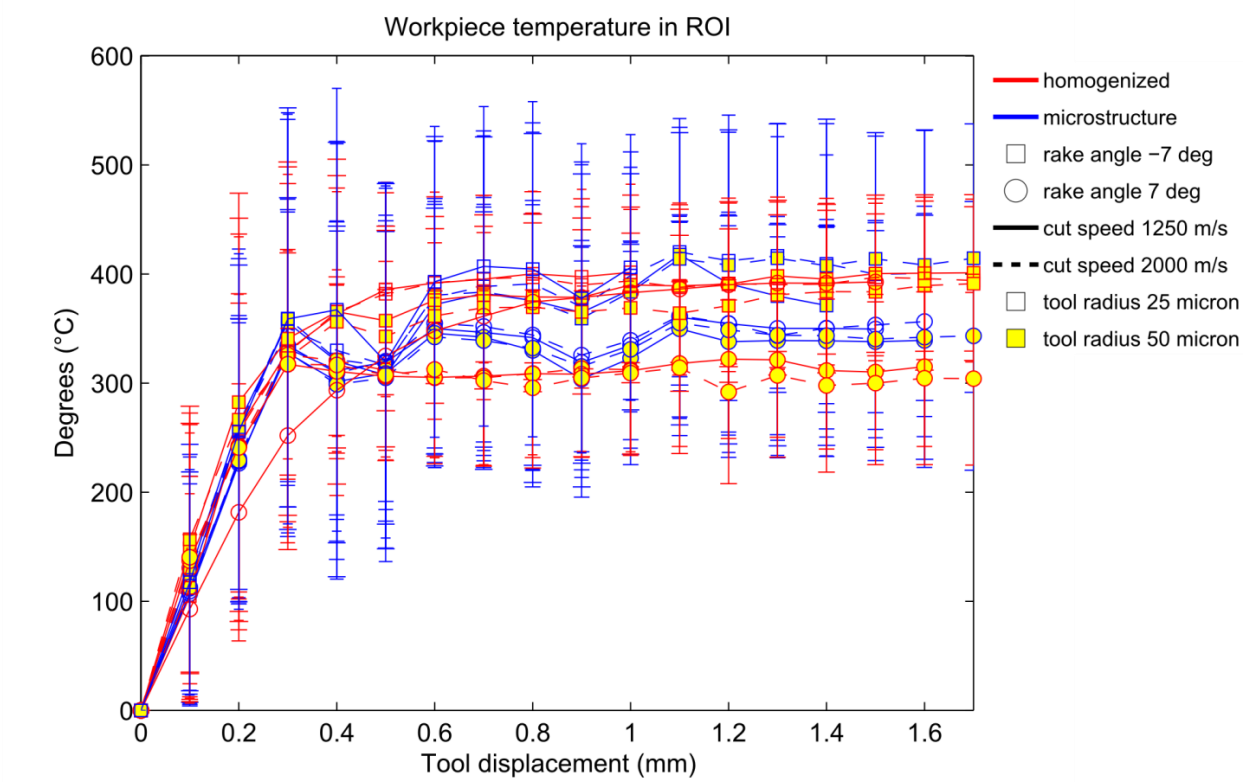

Fig. 13 Trend of the workpiece temperature plotted versus the tool displacement. The region of interest (ROI) is shown in Fig. 5a.

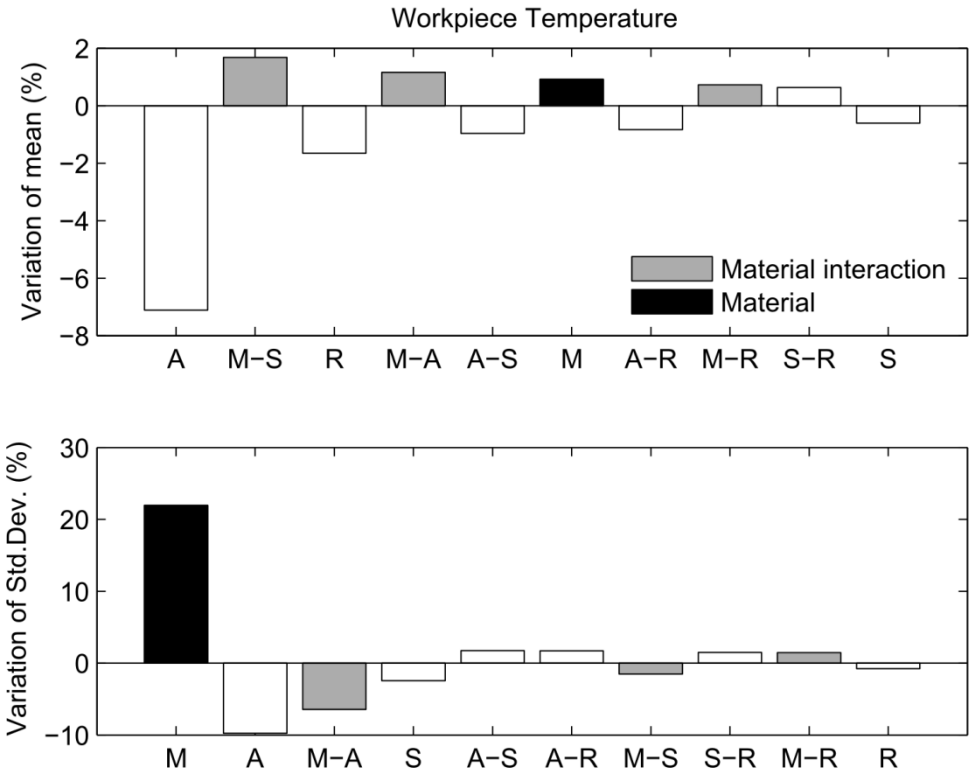

Fig. 14 Effects of main factors and their interactions on the workpiece temperature mean (top) and standard deviation (bottom). Material = M, rake angle = A, cutting speed = S and tool radius = R. Absolute variations are rank in decreasing order from left to right.

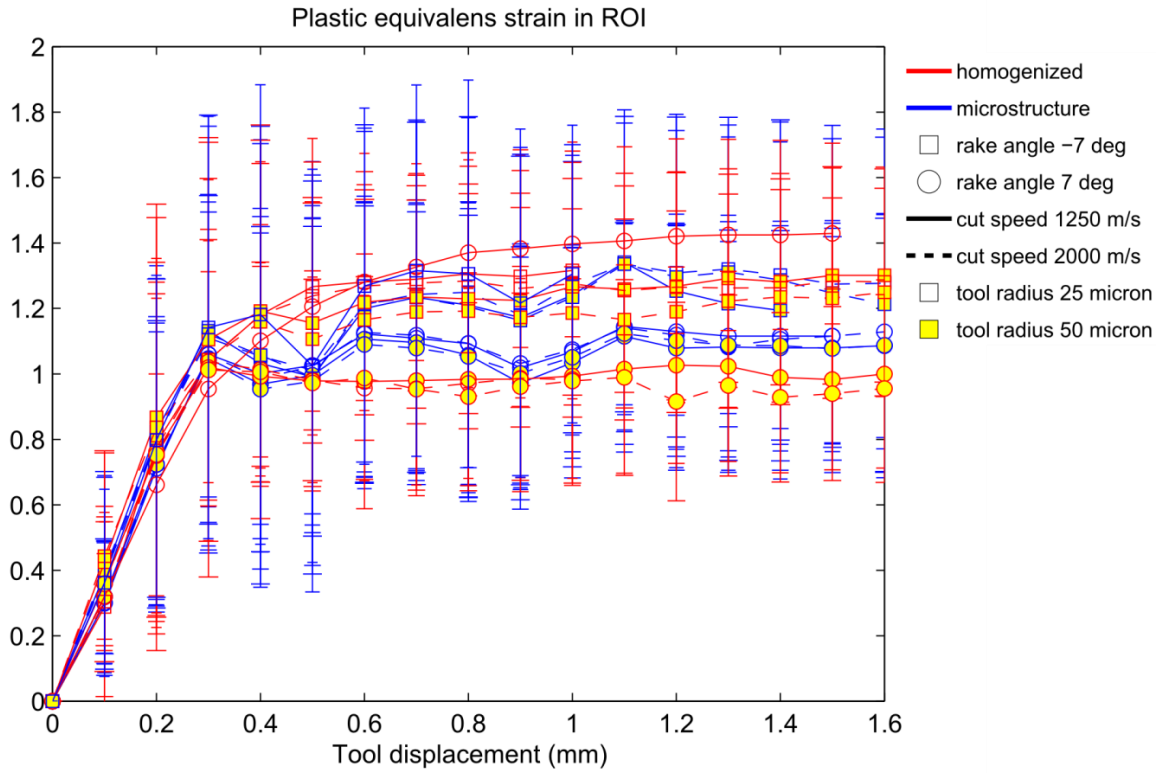

Fig. 15 Trend of the plastic equivalent strain plotted versus the tool displacement. The region of interest (ROI) is shown in Fig. 5a.

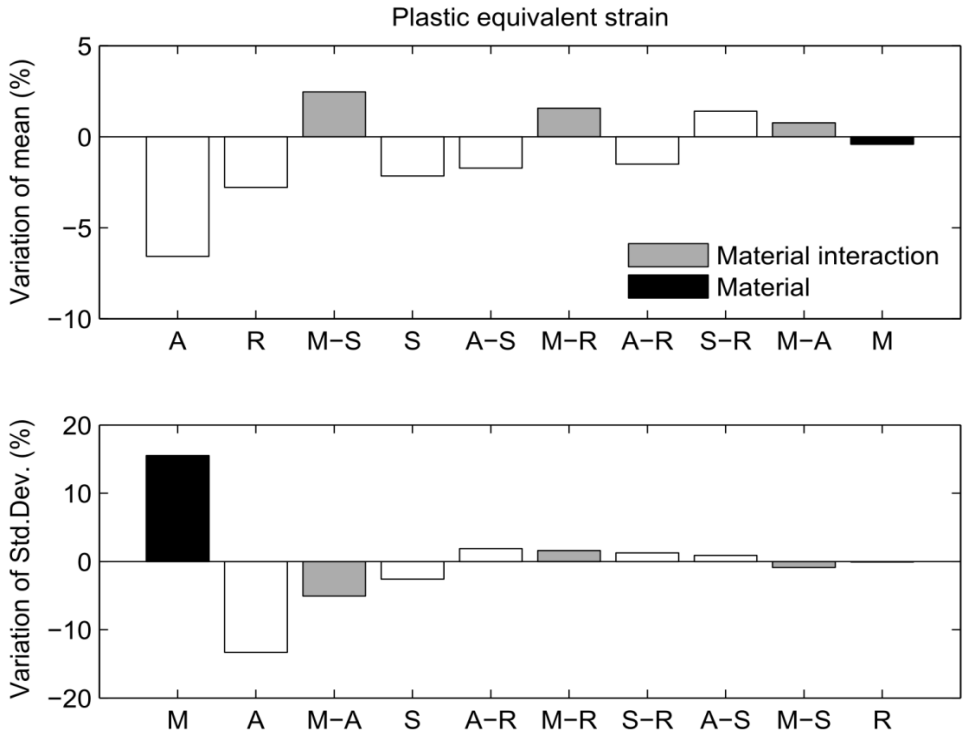

Fig. 16 Effects of main factors and their interactions on the plastic equivalent strain mean (top) and standard deviation (bottom). Material = M, rake angle = A, cutting speed = S and tool radius = R. Absolute variations are rank in decreasing order from left to right

7 TABLES

Table 1 Geometric and cutting parameters

Grain radius r_h (μm)	40
Workpiece length l (μm)	1020/2460
Workpiece height h (μm)	242
Layer thickness t (μm)	40
Number of layers	3
Tool size r_t (μm)	400
Tool edge radius r_e (μm)	50
Clearance angle α (deg)	18
Rake angle γ (deg)	-7
Cutting depth h_c (μm)	75
Tool speed V_c (m/s)	2

Table 2 General material properties

Property	AISI 1045[1]	Tungsten carbide tool[2]
Density ρ (kg/m^3)	7844	11900
Young's modulus E (GPa)	207	534
Poisson's ratio ν	0.3	0.22
Thermal expansion α (°C^{-1})	1.10^{-5}	
Specific heat c_p (J Kg^{-1} °C^{-1})	420	400
Thermal conductivity λ (W m^{-1} °C^{-1})	51	50

[1] extracted from Courbon et al. [16]
[2] extracted from Mabrouki and Rigal [13]

Table 3 Johnson-Cook parameters for ferrite and pearlite phases and homogeneous AISI 1045 steel

	A (MPa)	B (MPa)	n	m	C	$\dot{\varepsilon}_0$	T_{trans}(°C)	T_{melt} (°C)
Ferrite[1]	175	571	0.35	1.86	0.034	2.10^{-3}	21	1460
Pearlite[1]	750	593	0.33	1.10	0.011	2.10^{-3}	21	1460
AISI 1045[2]	546	487	0.25	1.22	0.015	2.10^{-3}	21	1460

[1] extracted from Abouridouane et al. [11]
[2] extracted from Duan et al. [17]

Table 4 Damage parameters in the Johnson-Cook failure criterion

Material	d_1	d_2	d_3	d_4	d_5	G_f
Ferrite / Pearlite[1]	0.06	3.31	-1.96	0.0018	0.58	0.

[1] extracted from Duan et al. [17], except of G_f

Table 5 Thermal/mechanical interaction properties

G_C (kJ/m^2)	21.33
$t_n^0 = t_t^0 \quad (N/mm^2)$	726
Friction coefficient	0.27
Fraction of dissipated energy due to friction	1
Thermal contact conductance $(W.m^{-2}C^{-1})$	10^4
Heat partition coefficient (tool/workpiece interface)	0.75

Table 6 Factorial study with the considered factors

Factor	**Abbr.**	**Level -1**	**Level 1**
Material	M	Homogeneous AISI 1045	Multiphase AISI 1045
Rake angle	A	-7 deg	7 deg
Cutting speed	S	1250 m/s	2000 m/s
Tool radius	R	25 micron	50 micron

Table 7 Table of simulations

	Factors level			
Run	**Material**	**Rake angle**	**Cutting speed**	**Tool radius**
1	-1	-1	-1	-1
2	-1	-1	-1	1
3	-1	-1	1	-1
4	-1	-1	1	1
5	-1	1	-1	-1
6	-1	1	-1	1
7	-1	1	1	-1
8	-1	1	1	1
9	1	-1	-1	-1
10	1	-1	-1	1
11	1	-1	1	-1
12	1	-1	1	1
13	1	1	-1	-1
14	1	1	-1	1
15	1	1	1	-1
16	1	1	1	1